

Coarse-Grained Refractory Composite Castables Based on Alumina and Niobium

Tilo Zienert,* Dirk Endler, Jana Hubáľková, Patrick Gehre, Michael Eusterholz, Torben Boll, Martin Heilmaier, Gökhan Günay, Anja Weidner, Horst Biermann, Bastian Kraft, Susanne Wagner, and Christos G. Aneziris

Niobium-alumina composite aggregates with 60 vol% metal content and with particle sizes up to 3150 μm are produced using castable technology followed by sintering, and a crushing and sieving process. X-Ray diffraction (XRD) analysis reveals phase separation during crushing as the niobium:corundum volume ratios is between 37:57 and 64:31 among the 4 produced aggregate classes 0–45, 45–500, 500–1000, and 1000–3150 μm . The synthesized aggregates are used to produce coarse-grained refractory composites in a second casting and sintering step. The fine- and coarse-grained material shows porosities between 32% and 36% with a determined cold modulus of rupture of 20 and 12 MPa, and E-moduli of 37 and 46 GPa, respectively. The synthesized fine-grained composites reached true strain values between 0.08 at 1100 $^{\circ}\text{C}$ and 0.18 at 1500 $^{\circ}\text{C}$ and the coarse-grained ones values between 0.02 and 0.09. The electrical conductivity for the fine-grained and the coarse-grained material is 448 ± 66 and $111 \pm 25 \text{ S cm}^{-1}$, respectively.

mixtures of refractory powders and pre-sintered aggregates up to a few millimeters in size, the extent of pores and pore networks has been adjusted in such materials, which improves the thermal shock resistance. Further improvements can be achieved by increasing the thermal conductivity and toughness of the material, and reducing the effective temperature difference by, e.g., electrical preheating of the material, which therefore needs an electrical conductivity. For this, coarse-grained refractory composites based on alumina–niobium or alumina–tantalum can be used^[1] that show promising high-temperature properties.^[2] In addition, by using pre-sintered refractory aggregates, the shrinkage on sintering can be drastically reduced in comparison to powder

1. Introduction

Refractory ceramics, i.e., alumina and spinel, are widely used as linings in metallurgical applications. These materials need to withstand harsh chemical and physical environments. Besides chemical corrosion of refractories in contact with liquid metals, lining refractories are altered by thermal shock due to crack initiation and crack growth on thermal cycling. By using

sintering. With that, monolithic refractory compounds can be produced using castable technology.^[3] Concerning the high cost and density of the refractory metals, the proposed refractory composites should be used only for the functional parts in refractory compounds, e.g., used as an electrical heater or as electrical conductive material to control wetting of melts on refractory linings.^[4] In addition, the metal content that satisfies the functional demand should be as low as possible.

T. Zienert, D. Endler, J. Hubáľková, P. Gehre, C. G. Aneziris
Institute of Ceramics, Refractories and Composite Materials
TU Bergakademie Freiberg
Agricolastr. 17, 09599 Freiberg, Germany
E-mail: tilo.zienert@licoo.de, tilo.zienert@ikfw.tu-freiberg.de

M. Eusterholz, T. Boll, M. Heilmaier
Institute for Applied Materials - Materials Science and Engineering
Karlsruhe Institute of Technology
Hermann-von-Helmholtz-Platz 1, 76344 Eggenstein-Leopoldshafen,
Germany

 The ORCID identification number(s) for the author(s) of this article can be found under <https://doi.org/10.1002/adem.202200296>.

© 2022 The Authors. Advanced Engineering Materials published by Wiley-VCH GmbH. This is an open access article under the terms of the Creative Commons Attribution-NonCommercial-NoDerivs License, which permits use and distribution in any medium, provided the original work is properly cited, the use is non-commercial and no modifications or adaptations are made.

DOI: 10.1002/adem.202200296

G. Günay, A. Weidner, H. Biermann
Institute of Materials Engineering
TU Bergakademie Freiberg
Gustav-Zeuner-Str. 5, 09599 Freiberg, Germany

B. Kraft, S. Wagner
Institute for Applied Materials - Ceramic Materials and Technologies
Karlsruhe Institute of Technology
Haid-und-Neu Str. 7, 76131 Karlsruhe, Germany

T. Zienert, D. Endler, C. G. Aneziris
Center for Efficient High Temperature Processes and Materials
Conversion
TU Bergakademie Freiberg
Winklerstraße 5, 09599 Freiberg, Germany

The feasibility to produce niobium–alumina aggregates and their usage in coarse-grained refractory composite castables was shown in our former work.^[5] Aggregates up to 3 mm were produced by a crushing and sieving process of casted and sintered fine-grained composite material with a composition of 65 vol% niobium. It was demonstrated that the most critical parameter of the composite's properties is the porosity, which is for castables directly related to their water demand to achieve a vibrational-assisted- or self-flowability.

In this work, the influence of reduced water contents on casted refractory composite properties is discussed. Properties are compared with the formerly produced material^[5] to show the influence of material selection and castable design.

2. Experimental Section

2.1. Composite Design Principles

By applying the principles 1) 'limit the influence of impurities on materials properties' and 2) 'limit the change of influencing parameters in comparison to our formerly synthesized castables^[5]' for material selection and castable design, the following constraints were defined. First, it was decided not use to organic additives for fine-grained castable mixtures to reduce the chance of carbide formation on sintering due to the presence of residual carbon related to a non-oxidic atmosphere on heat treatment. Therefore, only hydratable alumina was used as a binder additive and no organic-based dispersion additives were used for the synthesis of the fine-grained composite. The latter are normally used to control rheological behavior and water demand of the aqueous castable.^[3,6]

In addition, preliminary experiments showed that the alumina source has a strong influence on the metal–ceramic microstructure formation on sintering, which can be related to the chemistry, morphology, size, or porosity of the used powder particles. Keeping this in mind, only one alumina source was used for the fine-grained composite and only one other was used as fine-filler and sinter-active alumina for the coarse-grained mixture as already used before.^[1,5] Referring to,^[6] the castable can be classified as a cement-free one aiming at self-flowing or vibrational-assisted casting.

The second principle was set for the demand of comparison of refractory composite properties with former synthesized compounds.^[5] The recipe of the coarse-grained composite was, therefore, only slightly adjusted by additionally using a dispersing agent to reduce the water demand of the castable but the same binder system was used.

These design principles were creating some drawbacks related to the water demand and packing density of the aggregates of the castable and the porosity content of the sintered compound, which must be properly adjusted for a certain application. However, as this work aims at the general feasibility of refractory composite synthesis and base characterization of the material system without a certain application in mind, possible design drawbacks of the castables were accepted to study the influence of water content and material selection.

Table 1. Castable recipe for the fine-grained composite. The powder contents are given for the solid fraction, whereas the water content is given for the aqueous mixture.

Sample	Material	Massing	Amount	
			in mass%	in vol%
Solids	Niobium	1499.1	76.5	60.0
	CT9FG (alumina)	451.5	23.0	38.8
	Alphabond300 (binder)	9.9	0.5	1.2
Fine-w43	Water	225.9	10.3	43.3
Fine-w36	Water	166.8	7.8	36.1

Table 2. Determined particle sizes of the used raw materials and their chemistry.

Material	Particle size in μm				Purity	Main impurities
	d_{10}	d_{50}	d_{90}	d_{max}		
Niobium	9.1	30.8	64.9		99.95 wt% Nb	O, C, Ta
CT9FG	2.0	5.5	20.6		99.5 wt% Al_2O_3	Na, Fe, Si
CL370	0.2	0.5	5.8		99.7 wt% Al_2O_3	Na, Si, Fe, Ca
Alphabond300	4–8		30		88 wt% Al_2O_3 (min)	Ca, Na, Si

2.2. Composite Synthesis

Aggregates were synthesized with an intended niobium amount of 60 vol% as follows. First, fine-grained castable mixtures were produced according to the listed recipes in **Table 1** from raw materials (with determined particle sizes and chemistry as given in **Table 2**). Powders of niobium (EWG Wagner, Germany), the alumina CT9FG (Almatis, Germany), and the hydratable alumina binder Alphabond 300 (Almatis, Germany) were first dry mixed for one minute using an Eirich mixer (Gustav-Eirich Maschinenfabrik, Germany) followed by wet mixing for four minutes with step-wise water addition until almost self-flowability was achieved. This mixture was then filled in steel molds with dimensions of 25 mm × 25 mm × 150 mm by vibrational-assisted casting. After setting at room temperature for 48 h, the samples were demolded and dried for 24 h at 130 °C in air atmosphere. Afterward, the prisms were sintered at a temperature of 1600 °C for 4 h under a flowing argon atmosphere, which was purified by glowing magnesium chips. A furnace with a graphite inlay and graphite tools (Xerion, Germany) was used for sintering. Its chamber was evacuated three times and back-filled with argon before starting the heat treatment.

Two fine-grained castable batches were prepared—the first with a water content of 43 vol% and the second with 36 vol%, which are declared here as “fine-w43” and “fine-w36”, respectively. It should be noted that a few important parameters were different for these two batches due to constraints related to our laboratory setups. The fine-w43 samples were produced at room temperatures of 16–18 °C, whereas the second sample series was produced more close to standard room temperature at 20–21 °C. The temperature plays an important role in agglomeration of fine powders and the wetting behavior. It has, therefore, a strong influence on particle packing and final properties. In addition,

two different vibrating tables were used that also influence the setting of the powder particles during the casting process.

After sintering, the synthesized fine-grained prisms of batch “fine-w43” were broken and crushed using a jaw crusher (BB50, Retsch, Germany) with jaws made from hard metal (92% WC–8% Co). The jaws were moved with a speed of 650 min^{-1} using gap widths of 5, 3, 2, and 1 mm. After each crushing step, the crushed material was sieved into the four aggregate classes 0–45, 45–500, 500–1000, and 1000–3150 μm . Only the particles larger than 3150 μm were used in the next crushing step. It should be mentioned that the material of our finest aggregate class 0–45 μm was only obtained as residuals from the jaw crushing process, no further milling of coarser particles was done.

A selection of the synthesized composite aggregates was then used to produce an aqueous castable mixture, which was afterward casted, rested, dried, and sintered in the same way as the fine-grained material. The production route can be schematically visualized as follows. Casting: fine-grained composite $\xrightarrow{1600^\circ\text{C}}$ crushing: composite aggregates \rightarrow casting $\xrightarrow{1600^\circ\text{C}}$ coarse-grained composite.

2.3. Characterization

To evaluate our refractory composite in relation to technology parameters, physical and chemical properties were studied.

2.3.1. General Material Properties

Shrinkage, the envelope density, and porosity were determined on sintered prisms. For the latter two properties, the water-based Archimedes principle was used according to DIN EN 993-1:2019-03. Elastic constants were determined by the ultrasonic procedure (UKS-D device, GEOTRON-ELEKTRONIK, Germany) according to DIN EN 843-2:2006.

The electrical conductivity of the fine- and coarse-grained compound was determined on cutting cylinders in the same way as described before.^[5]

The particle size distribution of the synthesized aggregate classes 0–45, 45–500, and 500–1000 μm was determined using laser granulometry (Betttersizer S3 plus, 3P Instruments GmbH & Co. KG, Germany) and for the aggregate class 1000–3150 μm , it was determined by sieve analysis using sieves with mesh sizes of 2000, 2240, 2360, 2500, and 2800 μm . The aggregate’s skeleton density and porosity were determined using mercury intrusion porosimetry (AutoPore V 9600, Micromeritics Instrument Corp., USA) according to DIN ISO 15 901-1:2019-03.

2.3.2. Microstructure and Phase Assemblage

Cutted pieces of the composite samples were embedded in EpoMet embedding compound (Buehler, Germany), ground to SiC grit P4000, and subsequently polished with 3 and 1 μm diamond suspension. Final polishing was performed using a colloidal SiO_2 suspension.

Electron microscopy imaging and electron backscatter diffraction (EBSD) were performed using a Zeiss Auriga 60 dual-beam

scanning electron and focused ion beam microscope (Carl Zeiss AG, Germany) equipped with a backscatter electron (BSE) imaging detector, an EDAX octane silicon drift detector for energy-dispersive X-Ray spectroscopy (EDS) and an EDAX DigiView EBSD camera. EDS and EBSD were performed at 20 kV. Phase segmentation was performed with a self-programmed MATLAB script using BSE images recorded at different contrast levels. Areal phase fractions are considered to correspond to volume fractions due to isometry and isotropy of the microstructure.

The phase assemblage of the synthesized aggregates was studied by XRD (Empyrean, Malvern Panalytical GmbH, Germany) in combination with Rietveld refinement using HighScore Plus 4.8 (Malvern Panalytical B.V., the Netherlands) based on crystallographic information from the Inorganic Crystal Structure Database (ICSD) (FIZ Karlsruhe GmbH, Germany). XRD measurements were done using $\text{Cu-K}_{\alpha 1}$ radiation between 15 and 140° 2 θ with 0.0143° step size and an explosion time of 160 s/step.

2.3.3. Mechanical Testing

The cold modulus of rupture (CMOR) of the synthesized fine- and coarse-grained composite prisms was determined on the basis of DIN EN 993-6:1995-04 using a universal testing machine TIRAtest 28 100 (TIRA GmbH, Germany). To achieve a uniform distribution of bending moment, four-point bending setup with a support span of 125 mm, a load span of 62.5 mm, a pre-load of 20 N, and a loading rate of 150 N s^{-1} was applied. For these measurements, the composite prisms were used as fired and mounted so that the two almost parallel side planes of the prisms were connected with the support spans.

Quasi-static compression tests were performed to investigate the mechanical behavior of the synthesized fine- and coarse-grained refractory composite materials. The cylindrical specimens with a diameter of 12 mm and a height of 20 mm were drilled from sintered prisms. The compression tests were performed by an electromechanical, high-temperature testing machine (Z020, Zwick Roell, Germany) with a protective gas chamber (Maytec, Germany) integrated into the testing machine. The tests were conducted at four different temperatures (RT, 1100, 1300, and 1500 °C) with an initial strain rate of $7.5 \times 10^{-4} \text{ s}^{-1}$. To prevent the oxidation of the testing specimens, the test chamber was evacuated to 0.7 mbar vacuum and then filled with argon gas twice. After the evacuation process, the compression tests were performed under argon atmosphere and ambient pressure to reduce the possibility of oxidation of the testing specimens. The presence of oxygen was controlled by an O_2 sensor (Stange Elektronik, Germany). The heating of the specimens was carried out inductively via a medium-frequency induction generator (Hüttinger HF 5010, Germany) with a heating rate of 30 K s^{-1} and a water-cooled copper coil. The temperature was measured by a pyrometer (Sensortherm Metis MS09) with a wavelength of 0.9 μm and an emission coefficient of 0.93. Two susceptor plates between the upper and lower parts of the specimen and the load punches as well as a susceptor cage housing the specimens of an molybdenum–titanium–zirconium alloy TZM were used to ensure a homogenous temperature

distribution within the refractory composite specimens. Before heating, the lower piston was moved upward with a speed of 0.1 mm min^{-1} to apply a preload of 5 N onto the testing specimens. After reaching the testing temperature, the specimens were kept twenty minutes under the preload to acquire a homogeneous temperature distribution throughout the testing specimens. The tests were stopped when the testing machine had reached the maximum strain measurement value. Boron nitride was used as a lubricant to minimize friction between the TZM susceptor plates and the specimen (front and end faces).

3. Results

3.1. Fine-Grained Composite

Figure 1 shows scanning electron (SE) micrographs of the sintered fine-w43 composite. It can be seen that the raw materials

of alumina and niobium powders as well as pores, which are resulting from the casting process, were homogeneously mixed. In Figure 1b, a few niobium particles can be identified that contain grains of NbO. The latter was already present as an impurity phase in the raw material.

EDS maps were recorded at lower magnification (Figure 2) and in a magnified section (Figure 3) indicated by a red rectangle. Figure 3 permits a clear distinction of the element distributions in the Nb-rich particle and how they compare to the secondary electron contrast in Figure 3a. The difference in SE contrast of the regions marked “Nb” and “NbO” in Figure 3a and in the contrast difference in Figure 3c,d clearly indicate a variation in Nb and O concentrations. The EDS line scan shown in Figure 4 was performed along the red line placed in Figure 3a at a scan width of $2 \mu\text{m}$ and indicates the absence of Al and an almost 1:1 ratio of Nb and O. Hence, this phase is identified as NbO. The blue arrows in Figure 3a and 4 indicate the phase boundary between Nb and NbO.

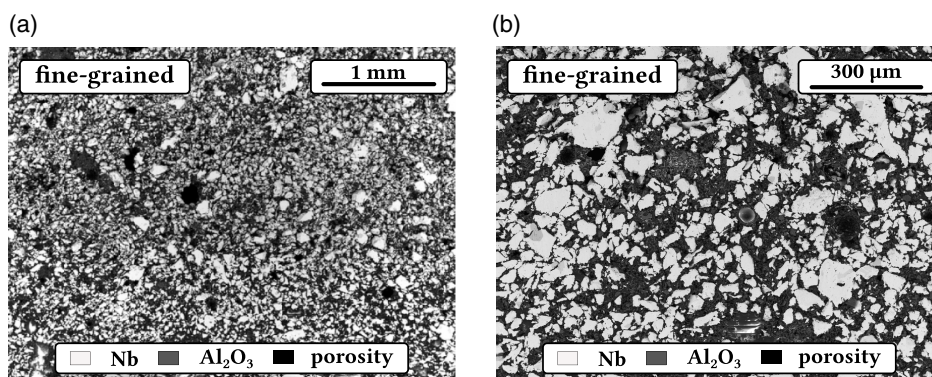


Figure 1. Backscatter electron (BSE) micrographs of the fine-grained composite “fine-w43” at different magnifications. Niobium and corundum appear in bright and dark gray contrast, respectively, with pores in black.

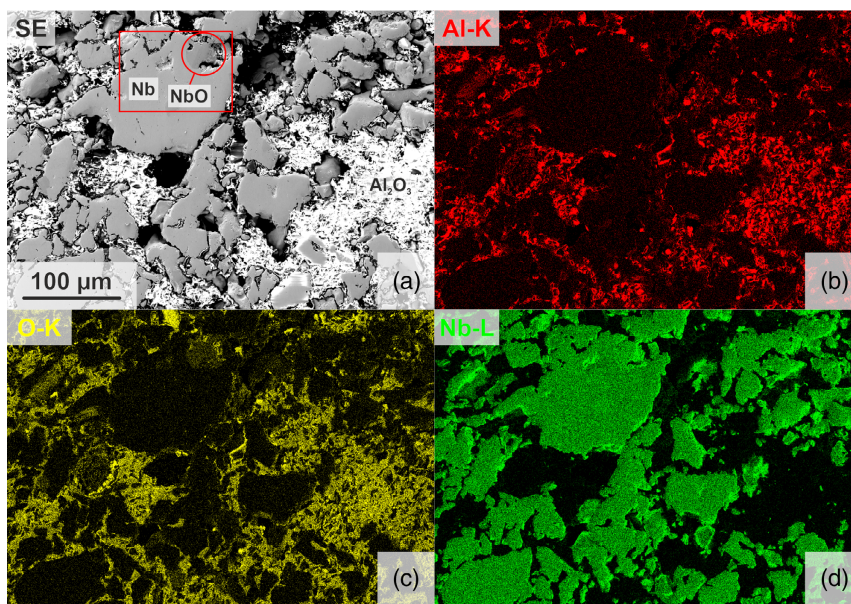


Figure 2. a) Scanning electron (SE) micrograph and energy-dispersive X-Ray spectroscopy (EDS) mapping analysis of: b) Al K, c) O K, and d) Nb L. The red rectangle indicates the region displayed in Figure 3. All images are taken at the same position and magnification.

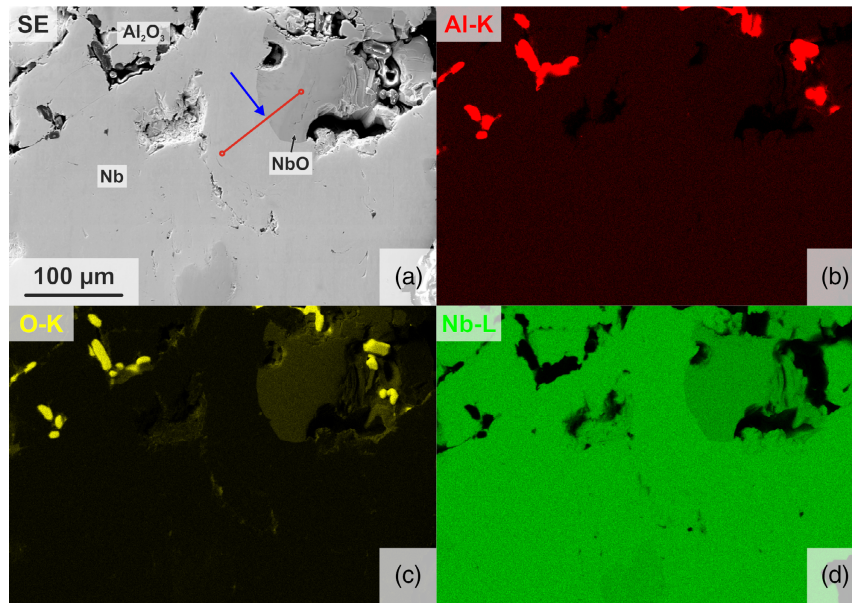


Figure 3. Close-up view of the top-left region in Figure 2 with: a) SE micrograph and EDS mapping analysis of: b) Al K, c) O K, and d) Nb L. e) Quantified EDS line scan along the red line placed in (a). The blue arrow indicates the location of the phase boundary in (a).

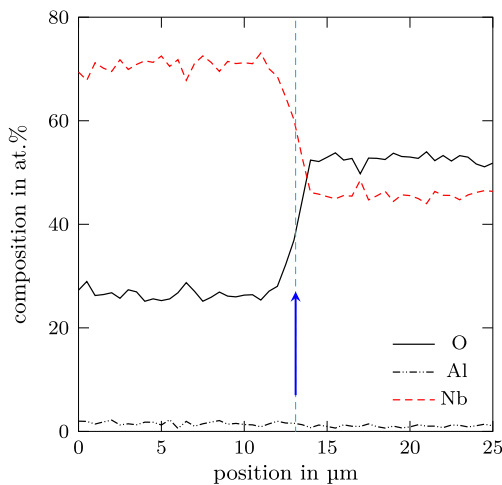


Figure 4. Quantified EDS line scan along the red line placed in a). The blue arrow indicates the location of the phase boundary in Figure 3a.

EBSD patterns in **Figure 5** were recorded for crystallographic identification of the phases present in the composite in the region detailed in **Figure 3**, including the area labeled NbO. The assigned crystal structures are provided in the figure caption and prominent zone axes are labeled according to the orientation determined by the EBSD software. In agreement with the elemental distributions obtained in **Figure 2** and **3**, the presence of NbO with the cubic crystal structure (space group 221, $a = 0.4211$ nm, NbO prototype) was confirmed besides the major phases niobium and corundum of the composite.

3.2. Synthesized Composite Aggregates

3.2.1. Morphology and Particle Size Distributions

The obtained characteristic particle sizes d_{10} , d_{50} , and d_{90} of the four aggregate classes are listed in **Table 3**. In comparison to the previously synthesized material,^[5] the characteristic particle sizes were very similar for the aggregate classes 0–45 and 500–1000 μm. The particle sizes of the aggregate class 45–500 μm of this work were more narrowly distributed than the ones of the formerly produced material as it is reflected by a d_{90} of 129 μm in comparison to $d_{90} = 325$ μm for the old composite fraction.^[5]

Figure 6 shows the particle size distributions in comparison to the ones reported in our previous work.^[5] In all aggregate classes up to 1000 μm, a certain amount of very fine particles with $0.1 \leq d \leq 0.5$ μm was always present. Above 1 μm, the particle size distributions were bimodal for the aggregate classes 0–45 and 45–500 μm as shown in **Figure 6a,b**, respectively. The first maximum was clearly detectable between 5 and 10 μm whereas the second one was always close to the respective d_{90} value. It should be noted that the first distribution maxima of this work were much more pronounced as compared to the previously reported ones. In contrast, the determined particle size distribution of the aggregate class 500–1000 μm is almost the same in both cases. The particle sizes were assumed to be linearly distributed between 1000 and 3150 μm in Ref. [5] The determined distribution of this work showed the same trend up to particle sizes of ≈ 2000 μm. Above and until 2500 μm, a slightly pronounced minimum was reached, followed by a strong increase indicating that a large amount (25%) of particles were obtained in the sieve fraction 2800–3150 μm.

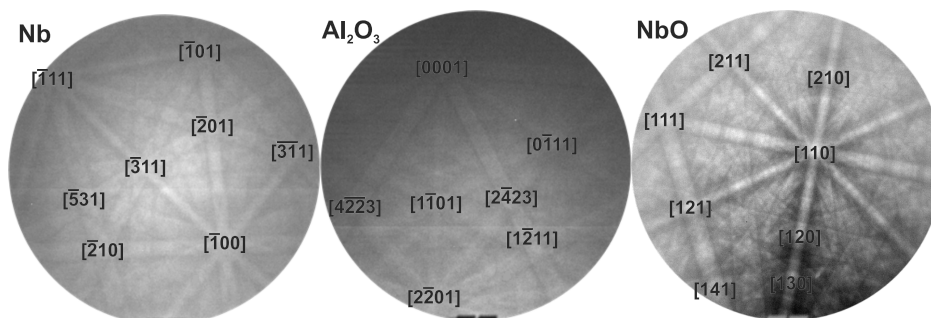


Figure 5. Indexed electron backscatter diffraction (EBSD) patterns of the three phases Nb (W prototype, space group 229), $\text{-Al}_2\text{O}_3$ (corundum prototype, space group 167), and NbO (NbO prototype, space group 221).

Table 3. Determined characteristic particle sizes of the synthesized aggregate classes.

Aggregate Class	Particle size in μm		
	d_{10}	d_{50}	d_{90}
0–45 μm	0.3	15.0	49.1
45–500 μm	2.6	44.0	129.0
500–1000 μm	269.2	496.0	717.4
1000–3150 μm	1208.6	2054.1	2996.7

3.2.2. Density and Porosity

Table 4 lists the determined values of density and porosity of the synthesized fine- and coarse-grained compounds as well as of the aggregates. With lowering the water content of the fine-grained castable, the open porosity of the samples was lowered by 4% to 32.3%. In comparison, the determined porosities of the sieve fractions 1000–3150 and 500–1000 μm were 32–33% very similar to the bulk values, whereas the porosity increased to 48% and 42% for the finer aggregate fractions 45–500 and 0–45 μm , respectively. The skeleton density of the aggregates was spread between 5.336 g cm^{-3} for 45–500 μm and 6.486 g cm^{-3} for 1000–3150 μm , which indicates differences in chemistry among the aggregate classes.

3.2.3. XRD Analysis

Rietveld analysis of the used niobium and CT9FG powder revealed the presence of several impurity phases. **Figure 7** shows an enlarged part of the diffraction pattern of the niobium raw material. Beside niobium (95.2 vol%, #ICSD-76 416^[7]) reflections, the ones of Nb_2C (2.5 vol%, #ICSD-31 973^[8]) and NbO (1.8 vol%, #ICSD-14 338^[9]) are clearly visible. The remaining reflections can be allocated with Nb_4C_3 (#ICSD-42 758^[10]), Nb_4N_3 (#ICSD-76 389), and Nb_6C_5 (#ICSD-63 503). These phases amount to less than 1 vol% of all phases.

The only detectable impurity phase in the used corundum source was $\text{Na}_2\text{O}\cdot 11\text{Al}_2\text{O}_3$ 1.3 vol%, #ICSD-15 970^[11], which is known as β -alumina. The corresponding diffraction pattern is shown in **Figure 8**.

The Rietveld analysis of the four aggregate classes showed that phase separation occurred during the crushing of the fine-grained material. The volume ratios of niobium:corundum were 57.2:37.1, 37.1:57.3, 63.8:30.6, and 55.8:39.4 for the aggregate classes from 0–45 μm to 1000–3150 μm . The two secondary phases NbO and $\beta\text{-Nb}_2\text{C}$ ^[13] were present in the aggregates. In addition, two different niobium and $\beta\text{-Nb}_2\text{C}$ phases were observed due to their respective differences in lattice parameters, which can be related to different chemistries of the respective niobium and $\beta\text{-Nb}_2\text{C}$ phases. As an example, the diffraction pattern of the aggregate class 500–1000 μm is shown in **Figure 9**. It should be noted that most of the impurity phases of the raw materials vanished or transformed during heat treatment under the used argon- and CO_2/CO -containing atmosphere. More details and a deeper discussion of the XRD results are given elsewhere.^[14]

3.3. Coarse-Grained Castable Recipe

The particle size distribution of solid mixtures was characterized by a cumulative sum curve or cumulative percent finer than particle size d CPFT(d).

$$\text{CPFT}_{\text{mod-DF}}(d) = 100\% \cdot \frac{d^{n(d)} - d_{\text{min}}^{n(d)}}{d_{\text{max}}^{n(d)} - d_{\text{min}}^{n(d)}} \quad (1)$$

using the particle-size dependent distribution modulus as defined in^[15] to

$$n(d) = n_{\text{min}} + d \cdot \frac{n_{\text{max}} - n_{\text{min}}}{d_{\text{max}}} \quad (2)$$

where n_{min} and n_{max} are the minimum and the maximum distribution modulus, respectively. For pure alumina-based castables, $n_{\text{min}} = 0.28$ and $n_{\text{max}} = 0.8$ were found to give the best properties in terms of flowability, density, and pore sizes.^[16] Therefore, our coarse-grained castable mixture (see **Table 5**) was designed to achieve these values as close as possible, depending on the determined particle-size distributions of each aggregate class. The relative density and CPFT of our mixture can be seen in **Figure 10a,b**, respectively. The determined values of the achieved distribution moduli were $n_{\text{min}} = 0.2727(25)$ and $n_{\text{max}} = 0.678(20)$.

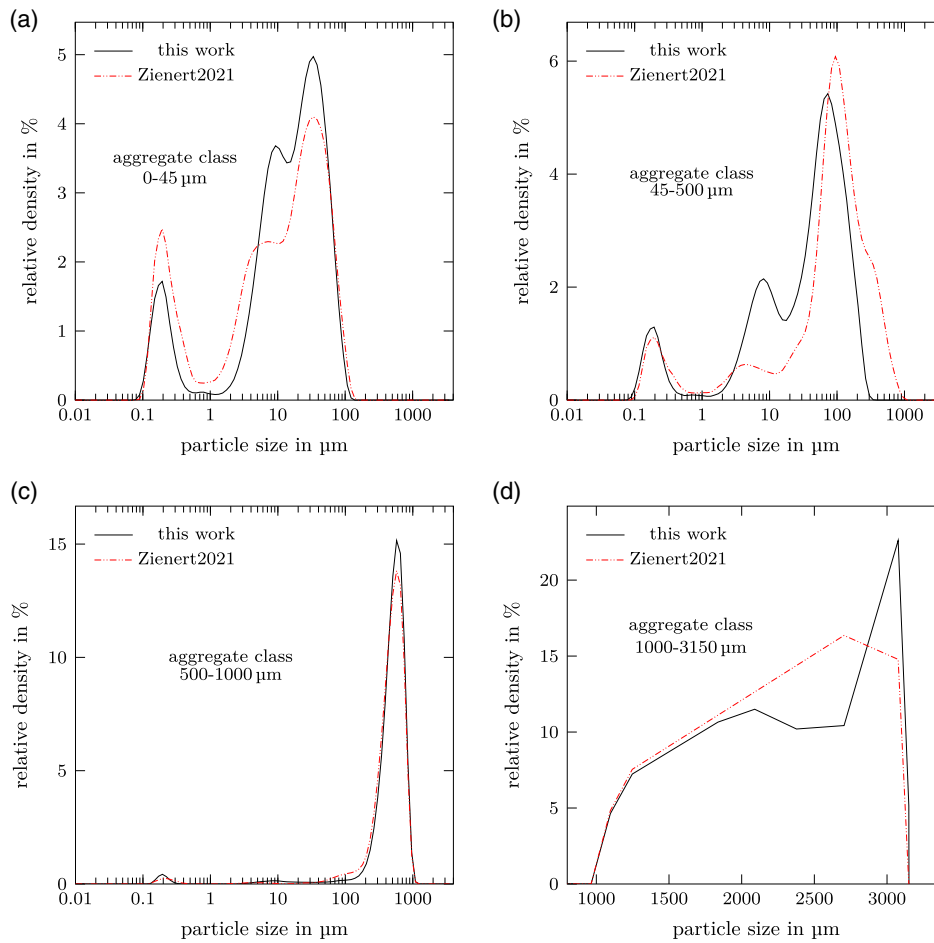


Figure 6. Comparison of determined particle size distributions of this work with the ones reported in Ref. [5]: a) 0–45 μm , b) 45–500 μm , c) 500–1000 μm , and d) 1000–3150 μm .

Table 4. Determined values of shrinkage; the envelope density ρ_b and the open porosity π_a according to DIN EN 993-1:2019-03, the skeleton density ρ_s and the porosity ε according to DIN ISO 15 901-1:2019-03 of the synthesized aggregates as well as the sintered fine-grained and coarse-grained composites. If applicable, values are given as mean value \pm standard deviation.

	Shrinkage	Archimedes		MIP		XRD	
	in %	ρ_b in g cm^{-3}	π_a in %	ρ_s in g cm^{-3}	ε in %	ρ in g cm^{-3}	
Fine-w43	2.65 ± 0.29	4.27 ± 0.11	36.31 ± 1.37				
Fine-w36	2.09 ± 0.12	4.46 ± 0.14	32.26 ± 0.91				
Aggregate fraction from fine-w43							
0–45 μm				6.035	41.74	3.516	6.796
45–500 μm				5.336	48.31	2.758	5.883
500–1000 μm				6.408	32.75	4.310	7.087
1000–3150 μm				6.486	31.84	4.421	6.692
Coarse-grained composite	0.79 ± 0.21	4.18 ± 0.04	34.29 ± 0.56				

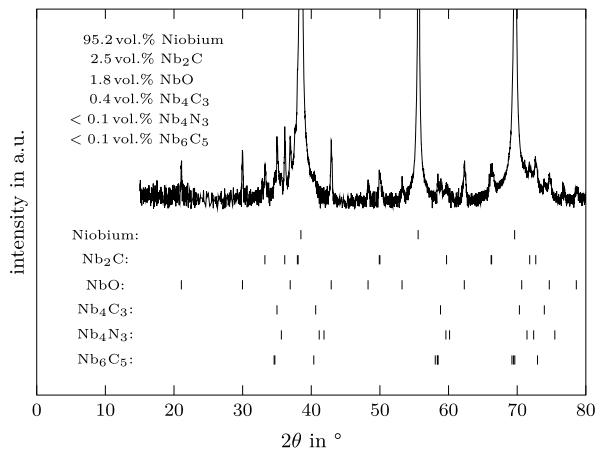


Figure 7. X-Ray diffraction (XRD) pattern of the niobium raw material with marked reflections for the phases niobium (#ICSD-76 416^[7]), Nb₂C (#ICSD-31 973^[8]), NbO (#ICSD-14 338^[9]), Nb₄C₃ (#ICSD-42 758^[10]), Nb₄N₃ (#ICSD-76 389), and Nb₆C₅ (#ICSD-63 503).

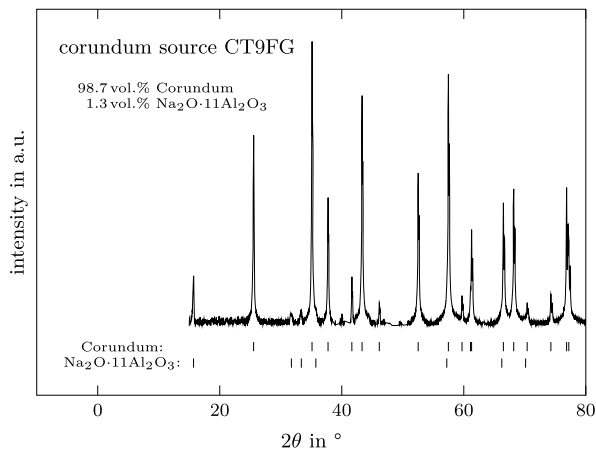


Figure 8. XRD pattern of the main corundum source CT9FG with marked reflections for the phases corundum (#ICSD-73 725^[12]) and Na₂O·11Al₂O₃ (#ICSD-15 970^[11]).

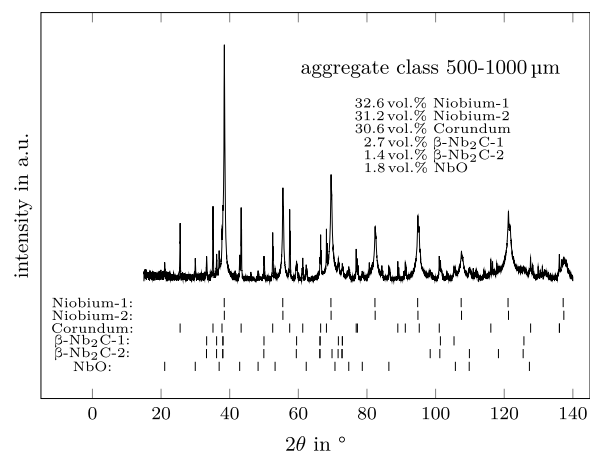


Figure 9. XRD pattern of aggregate class 500–1000 μm with marked reflections for the phases niobium (#ICSD-76 416^[7]), corundum (#ICSD-73 725^[12]), β-Nb₂C,^[13] and NbO (#ICSD-14 338^[9]).

Table 5. Coarse-Grained castable recipe. Amounts of powders and the synthesized aggregates were calculated for the solid content only. The amount of water was calculated for the mixture of solids + water.

Material	Density	Mass	Amount	
	in g cm ⁻³	in g	in mass%	in vol%
Niobium	8.46	149.9	4.62	2.14
0–45 μm	3.516	32.6	1.01	1.12
45–500 μm	2.758	656.2	20.24	28.74
500–1000 μm	4.310	643.6	19.86	18.04
1000–3150 μm	4.421	1433.5	44.22	39.16
CL370 (alumina)	4.013	250.6	7.73	7.54
Alphabond300 (binder)	2.781	75.1	2.32	3.26
Water	1	258.5	7.39	23.79
Castament VP95L		9.7		

In our recent work on a 65 vol% metal-containing niobium-alumina composite,^[5] distribution moduli of $n_{\min} = 0.2716(30)$ and $n_{\max} = 0.295(24)$ were obtained due to material limitations. The lower n_{\max} value in comparison to the one of this work is due to the lower amount of aggregates with particle sizes larger than 1000 μm. The differences in the particle size distributions between our recent mixture^[5] and the current one can be seen in **Figure 11**. The latter had fewer particles with $200 \leq d \leq 1000 \mu\text{m}$ than in Ref. [5], which resulted in a particle size distribution much closer to the intended one.

Figure 12 shows the particle size distributions for the particle range $\leq 200 \mu\text{m}$ of the fine- and coarse-grained castable mixture. In case of the fine-grained mixture (**Figure 12a**), most of the alumina particles (CT9FG) were in the range of 1–10 μm. For the coarse-grained mixture, the alumina source CL370 (consisting of 1.5 vol% β-alumina) was used additionally, which added a significant amount of very fine particles with $d \leq 1 \mu\text{m}$ to the powder blend (**Figure 12b**). Together with the very fine part of the composite aggregates, the amount of particles with $d \leq 1 \mu\text{m}$ summed up to 8.7 vol% for the coarse-grained mixture in comparison to 2.1 vol% for the fine-grained one. These very fine particles were the most active component during the sintering process and did therefore most influence microstructure formation and final mechanical properties.

3.4. Coarse-Grained Composite

After sintering, the open porosity of the compound samples was determined to be $\approx 34\%$ (see **Table 4**), which is within the range of the two investigated fine-grained composites. Using pre-sintered aggregates in the coarse-grained castable lead to a shrinkage of only 0.8% in comparison to 2.1–2.7% of the fine-grained composites (see **Table 4**).

The microstructure displayed in **Figure 13** was more heterogeneous in comparison to the fine-grained sample shown in **Figure 1**. It comprised several crushed granule regions appearing in bright BSE contrast, separated by dark channels of fine-grained alumina. Pores can be detected in the regions high

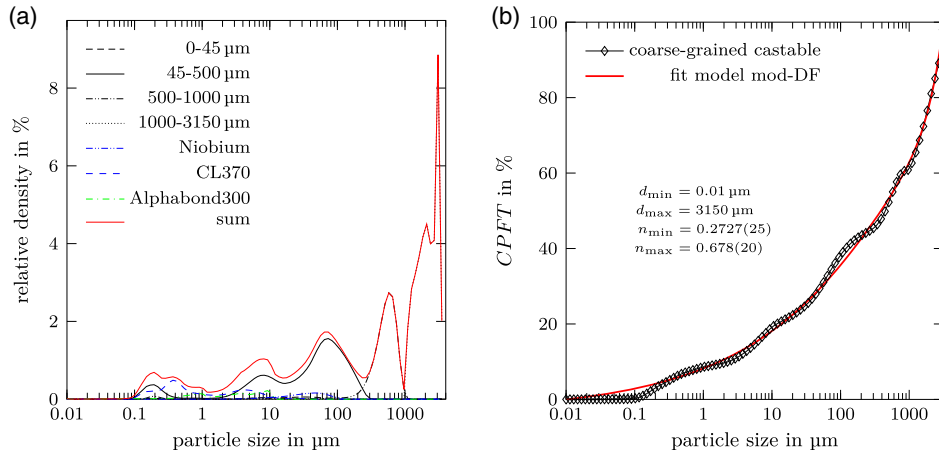


Figure 10. a) Particle size distributions of the used castable components as they contribute to the castable's particle size distribution (calculated sum distribution); b) CPFT of the particles of the coarse-grained castable together with the results of the fit using the modified Dinger–Funk distribution model (see Equation (1)).

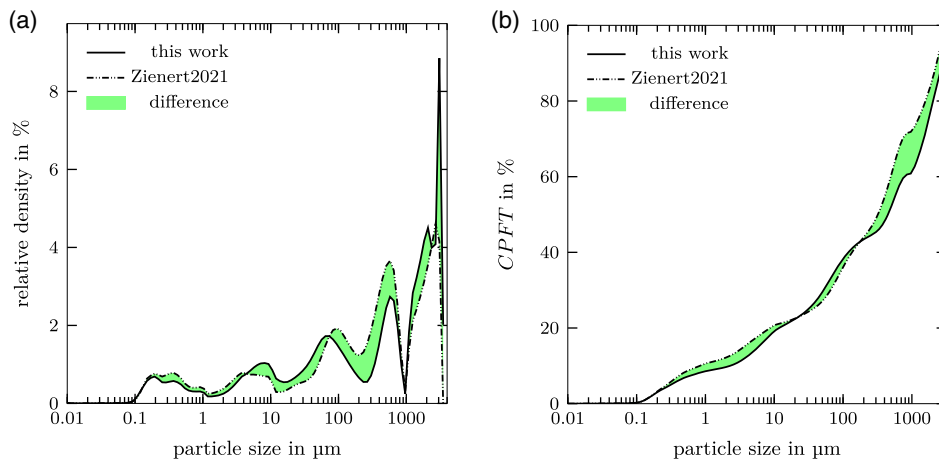


Figure 11. Comparison with the castable mixture reported in Ref.[5] a) Particle size distributions ; b) CPFT of the particles of the coarse-grained castable.

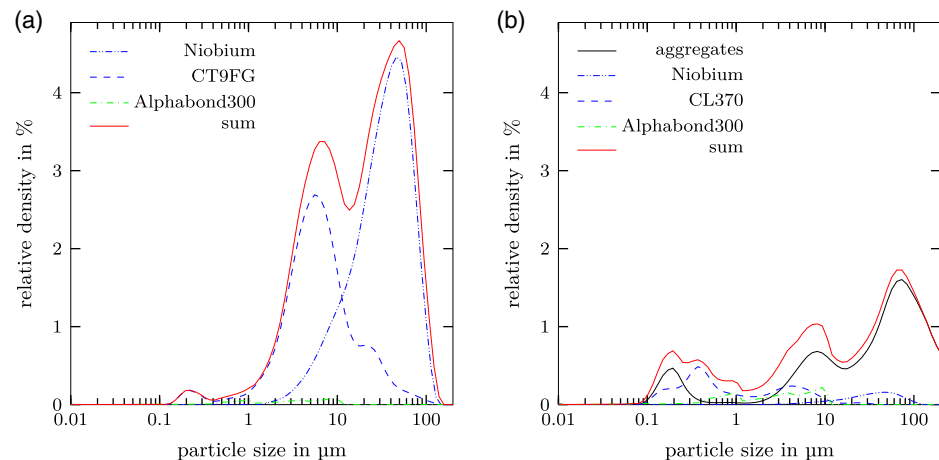


Figure 12. Particle size distributions of the two castable mixtures for 0–200 μm : a) fine-grained and b) coarse-grained.

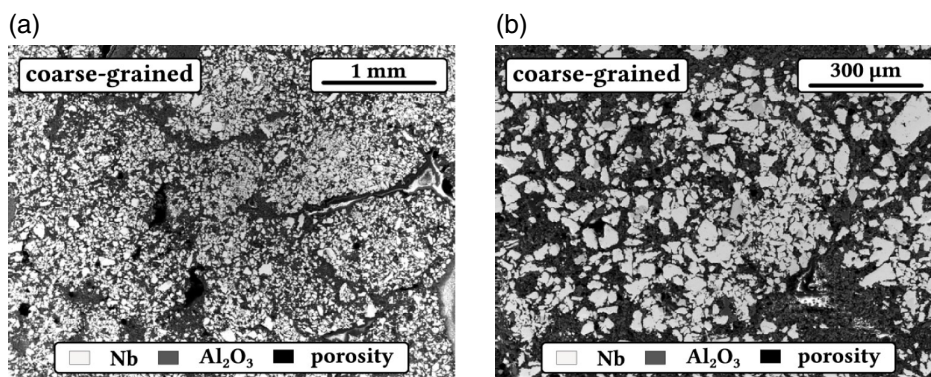


Figure 13. BSE micrographs of the coarse-grained composite at different magnifications. Niobium and corundum appear in bright and dark contrast, respectively.

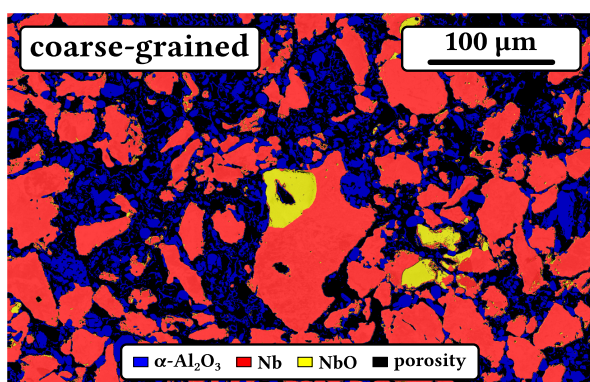


Figure 14. Phase segmentation from BSE imaging based on grey level binarization. The phases Nb, α - Al_2O_3 and NbO, and porosity are indicated by red, blue, yellow, and black color, respectively.

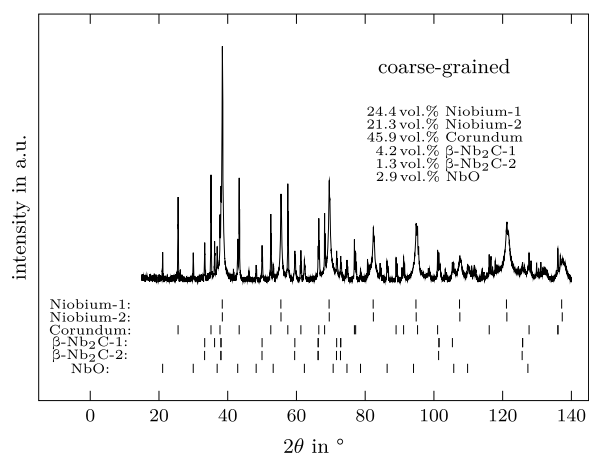


Figure 15. XRD pattern of the coarse-grained refractory composite with marked reflections for the phases niobium (#ICSD-76 416^[7]), corundum (#ICSD-73 725^[12]), β - Nb_2C ,^[13] and NbO (#ICSD-14 338^[9]).

in alumina and partially show bright charging contrast resulting from the embedding compound.

Figure 14 depicts a phase map obtained by segmentation of BSE images recorded at different contrast levels. This representative section of the microstructure exhibits the agglomeration of Nb

(red) particles of a few microns up to above 100 μm in size, surrounded by fine alumina particles (blue). The porosity in the image amounted to about 30%; NbO was present as a minority phase.

XRD/Rietveld analysis of the powdered coarse-grained composite (see **Figure 15**) showed a slightly increase of secondary phases during the second sintering step in comparison to the fine-grained material. The β - Nb_2C content increased to 5.5 vol% and NbO was present with ≈ 3 vol%.

3.5. Comparison of Mechanical Properties and Elastic Constants of the Fine- and Coarse-Grained Composites

Boxplots of the determined values for the synthesized fine- and coarse-grained samples of the elastic constants E , G , and ν can be seen in **Figure 16** and the ones for CMOR in **Figure 17**, the corresponding median values are listed in **Table 6**. The values of Young's modulus and shear modulus of the fine-grained castable samples with the lower water content were, respectively, 42 and 17 GPa $\approx 10\%$ larger than the ones for the mixture with the higher water (and higher porosity) content. However, these values were roughly fifty percent of the ones determined for our last composite with 65 vol% niobium.^[5] Interestingly, E and G increased further by 10% in case of the coarse-grained compound reaching 45.5 and 18.5 GPa, respectively, which are very similar to the ones of the former coarse-grained composite.

In contrast, the cold modulus of rupture was the highest for the fine-grained mixture with the high water content and lowest for the coarse-grained sample.

3.6. High-Temperature Compressive Strength

Figure 18 shows true stress versus true strain curves of the fine-w43 and the coarse-grained composite materials obtained under compressive load at four different temperatures and at a strain rate of $7.5 \times 10^{-4} \text{ s}^{-1}$ (depicted from^[17]). As seen in **Figure 18a**, the fine-grained material reached at room temperature (RT) the highest ultimate compressive strength but failed in a brittle manner. However, at elevated temperatures, the material exhibited ductile behavior at decreasing flow stress. Thus, a compressive strain of 0.10 and 0.18 was obtained at 1300 $^\circ\text{C}$ and

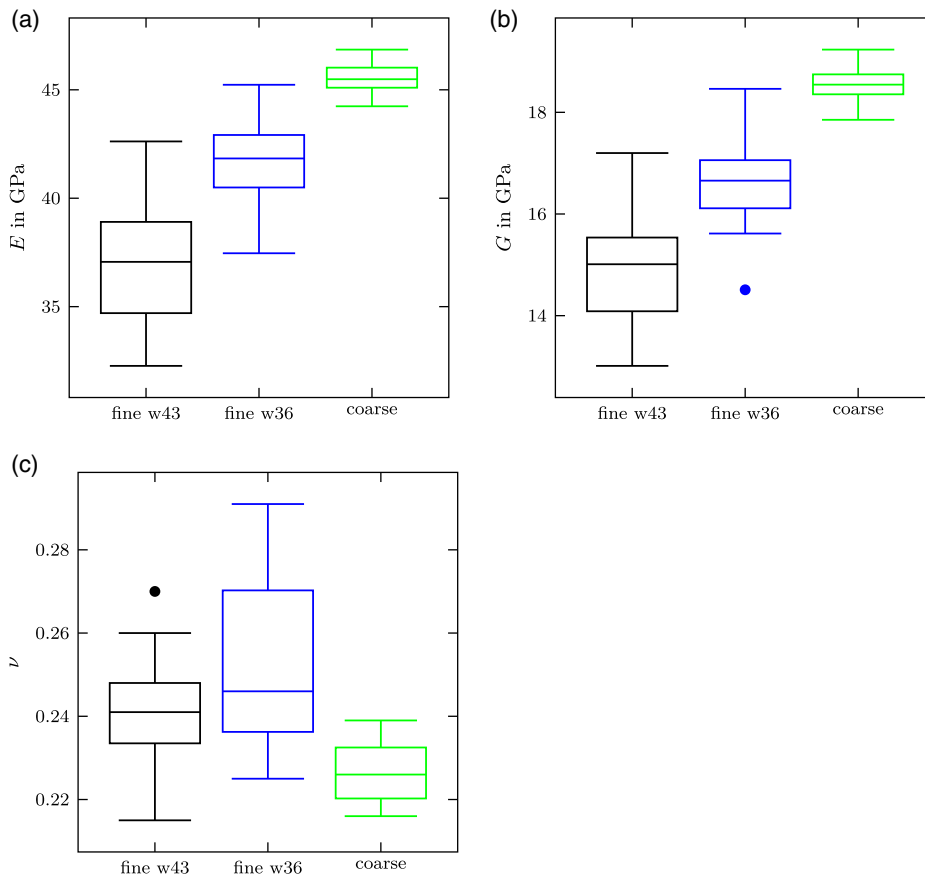


Figure 16. Determined elastic constants: a) E , b) G , and c) ν for the two fine-grained composites and for the coarse-grained one.

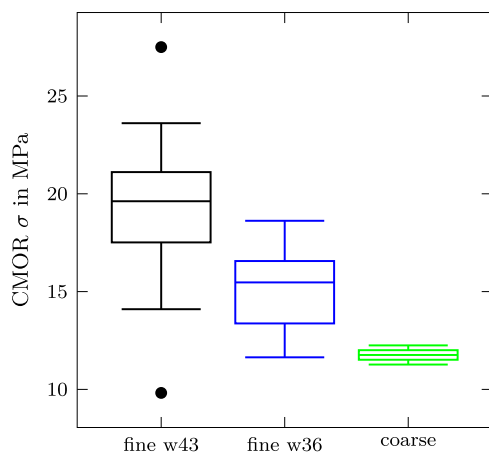


Figure 17. Determined values of the cold modulus of rupture for the fine- and coarse-grained composite samples.

1500 °C, respectively. Figure 18b shows the true stress versus true strain curves for the coarse-grained composite at the same temperatures and strain rate. It is obvious that higher flow stresses at lower plasticity were obtained for the coarse-grained

Table 6. Determined median values of the elastic constants Young's modulus E , shear modulus G , and Poisson's ratio ν (32 fine-grained "w43", 14 fine-grained "w36", and 8 coarse-grained samples) and of the four-point bending strength σ of the sintered fine-grained (22 samples "w43" and 14 ones "w36") and coarse-grained (2 samples) composites.

	Elastic constants			CMOR
	E in GPa	G in GPa	ν	σ in MPa
Fine-w43	37.1	15.0	0.241	19.5
Fine-w36	41.8	16.7	0.246	15.5
Coarse-grained	45.5	18.5	0.226	11.8

material compared to the fine-grained material. Thus, true strain values of only 0.03 and 0.09 were reached at 1300 °C and 1500 °C. Nevertheless, the coarse-grained material achieved higher strength and failed not completely in a brittle manner, as a plasticity of about 9% was observed at higher temperatures.

Table 7 shows the yield stresses and rupture stresses (in MPa) obtained at a strain rate of $7.5 \times 10^{-4} \text{ s}^{-1}$ for the fine- and coarse-grained composite. The compressive yield stresses of the fine- and

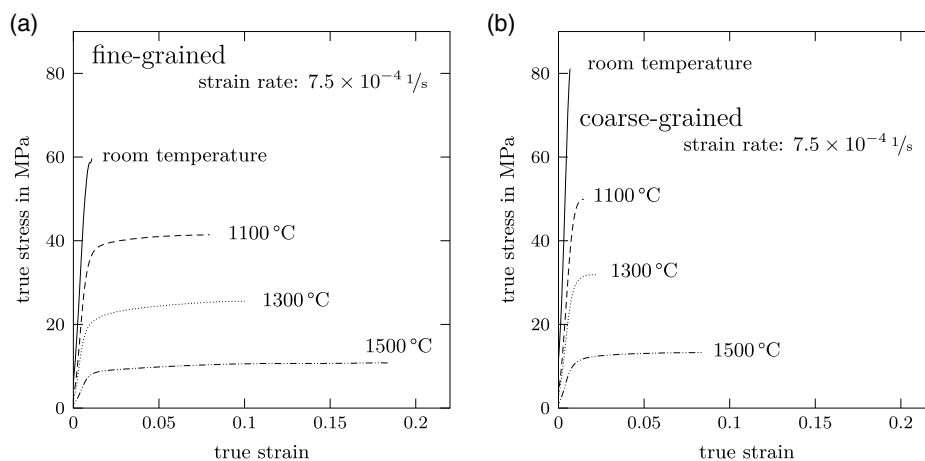


Figure 18. True stress–true strain curves of: a) fine-grained and b) coarse-grained specimens under compressive load for four temperatures depicted from.^[17]

Table 7. Yield stresses or rupture stress (in MPa) obtained at a strain rate of $7.5 \times 10^{-4} \text{ s}^{-1}$ for the fine-w43 and the coarse-grained composites.

Sample	RT	1100 °C	1300 °C	1500 °C
Fine-w43	48.9	29.7	16.4	6.5
Coarse-grained	80.3	40.2	23.4	9.3

coarse-grained composite materials show a pronounced yet expected dependence on the temperature at a constant strain rate. The yield stresses achieved by coarse-grained composite materials are significantly higher compared to fine-grained materials at all temperatures. The difference in the yield stresses between coarse- and fine-grained materials can be related to different porosities.^[17]

3.7. Electrical Conductivity

The electrical conductivity of the fine-grained composite fine-w43 was determined to $448 \pm 66 \text{ S cm}^{-1}$ and for the coarse-grained one to $111 \pm 25 \text{ S cm}^{-1}$. These values are one magnitude of order larger than those of the previously investigated fine-grained composites with 65 vol% Nb synthesised from powder mixing and pressing.^[5] Using castables for composite synthesis resulted in a more homogeneous microstructure without pronounced anisotropy effects. Even with 32–36% open porosity, the composites with $\approx 60 \text{ vol% Nb}$ showed electrical conductivities only two orders of magnitude below the reported ones of pure niobium.^[18] The decreased electrical conductivity of the coarse-grained material in comparison to the fine-grained one can be related to higher porosity and a slightly lower metal content due to the additional alumina binder content.

4. Conclusions and Outlook

The temperature had a strong influence on the water demand of the fine-grained castables, which was reduced by 8 vol% by increasing the mixing temperature by $\approx 3\text{--}4 \text{ K}$. With needing less water, the open porosity was lowered by 4%

reaching 32%, which is still much more than the usual 10–20% of refractory castables. To further increase the density of the fine-grained castables, their packing density must be improved by using a larger amount of fines to fill pores with a diameter less than $10 \mu\text{m}$.

Comparing the mechanical properties of the fine-grained and coarse-grained samples revealed larger values in yield stress at all investigated temperatures for the coarse-grained ones. For both composites, the determined open porosity was almost the same with $\approx 35 \text{ vol%}$, differences were arising from composition in terms of chemistry and aggregate types. It can be concluded that the higher amount of highly sinterable particles with $d \leq 1 \mu\text{m}$ resulted in a stronger bonding between the particles on a micro-scale without changing overall density. This positive bonding effect seems to be much stronger than negative effects related to porosity as shown by the determined values of elastic constants. With lowering the water content of the fine-grained castable mixture, the open porosity decreased by 4% and the values of Young's modulus and shear modulus increased by $\approx 10\%$. These two elastic constants increased even by $\approx 20\%$ in the case of the coarse-grained composite despite the porosity being only 2% lower than the one of the fine-grained mixture with the higher water content.

The arrangement of pores and pore networks was also relevant besides the absolute value of porosity. They were much more homogeneously distributed for the fine-grained composite in comparison to the coarse-grained one. This leads to a smaller failure probability in compression tests and to larger achievable strain values, which is also reflected by the results of the four-point bending measurements.

The mechanical strength of coarse-grained material will be further improved by using more dense aggregates, which will be synthesized by cold isostatic pressing and sintering or using field-assisted sintering technique that resulted in our material in porosity values of 25% and 5%,^[19] respectively. However, in contrast, the porous material can be used to reduce internal stress due to its ability to show strain values up to 25%.^[17] For this purpose, it is planned to investigate layered materials based on layers of alumina and niobium-alumina composite, respectively.

Acknowledgements

This research was funded by the German Research Foundation (DFG) within the Research Unit FOR 3010 (Project number: 416817512). The X-Ray diffractometer was acquired through the “Major Research Instrumentation” funding programme of the German Research Foundation (DFG), reference number: INST 267/157-1 FUGG (Project number: 395259190). Parts of this work were financed through public funds from the Federal Ministry of Education and Research and the State of Saxony (SN0390002) and with the support of the Karlsruhe Nano Micro Facility (KNMFi, www.knmf.kit.edu), a Helmholtz Research Infrastructure at Karlsruhe Institute of Technology (KIT, www.kit.edu) (reference numbers: HE 1872 40-1, BO 5154 1-1).

Open Access funding enabled and organized by Projekt DEAL.

Conflict of Interest

The authors declare no conflict of interest.

Data Availability Statement

The data that support the findings of this study are available from the corresponding author upon reasonable request.

Keywords

castable, electrical conductivity, high-temperature mechanical properties, refractory composite

Received: March 1, 2022

Revised: April 11, 2022

Published online: May 14, 2022

[1] T. Zienert, M. Farhani, S. Dudczig, C. G. Aneziris, *Ceram. Int.* **2018**, *44*, 16809.

- [2] A. Weidner, Y. Ranglack-Klemm, T. Zienert, C. G. Aneziris, H. Biermann, *Materials* **2019**, *12*, 3927.
- [3] A. P. Luz, M. A. L. Braulio, V. C. Pandolfelli, *Refractory Castable Engineering*, volume 1 of F.I.R.E. Compendium Series, Göller Verlag, Baden-Baden, Germany **2015**, ISBN 9783872640048.
- [4] C. G. Aneziris, M. Hampel, *Int. J. Appl. Ceram. Technol.* **2008**, *5*, 469.
- [5] T. Zienert, D. Endler, J. Hubáľková, G. Günay, A. Weidner, H. Biermann, B. Kraft, S. Wagner, C. G. Aneziris, *Materials* **2021**, *14*, 6543.
- [6] W. E. Lee, W. Vieira, S. Zhang, K. Ghanbari Ahari, H. Sarpoolaky, C. Parr, *Int. Mater. Rev.* **2001**, *46*, 145.
- [7] J. W. Edwards, R. Speiser, H. L. Johnston, *J. Appl. Phys.* **1951**, *22*, 424.
- [8] K. Yvon, H. Nowotny, R. Kieffer, *Monatsh. Chem. Verw. Teile Anderer Wiss.* **1967**, *98*, 34.
- [9] A. L. Bowman, T. C. Wallace, J. L. Yarnell, R. G. Wenzel, *Acta Crystallogr.* **1966**, *21*, 843.
- [10] V. G. Zubkov, L. B. Dubrovskaya, P. V. Gel'd, V. A. Tskhai, Y. A. Dorofeev, *Dokl. Akad. Nauk SSSR* **1969**, *184*, 874, (in Russian).
- [11] C. A. Beevers, M. A. S. Ross, *Z. Kristallogr.* **1937**, *97*, 59.
- [12] E. N. Maslen, V. A. Streltsov, N. R. Streltsova, N. Ishizawa, Y. Satow, *Acta Crystallogr. Sec. B* **1993**, *49*, 973.
- [13] N. Terao, *Jpn. J. Appl. Phys.* **1964**, *3*, 104.
- [14] T. Zienert, D. Endler, N. Brachhold, M. Weiner, M. Schmidtchen, U. Prah, C. G. Aneziris, *Adv. Eng. Mater.* **2022**, Under review, adem.202200407.
- [15] J. Fruhstorfer, *Mater. Today Commun.* **2019**, *20*, 100550.
- [16] J. Fruhstorfer, C. G. Aneziris, *Sci. Technol.* **2014**, *05*, 155.
- [17] G. Günay, T. Zienert, D. Endler, C. G. Aneziris, H. Biermann, A. Weidner, *Adv. Eng. Mater.* **2022**, in press, adem.202200292.
- [18] I. L. Shabalin, *Ultra-High Temperature Materials I*, Springer Science+Business Media Dodrecht, Heidelberg, New York, London **2014**, ISBN 978-94-007-7586-2.
- [19] B. Kraft, S. Wagner, M. J. Hoffmann, *Adv. Eng. Mater.* **2022**, Submitted, this issue.